International Journal of Heat and Fluid Flow 71 (2018) 275–287

Contents lists available at ScienceDirect

International Journal of Heat and Fluid Flow

journal homepage: www.elsevier.com/locate/ijhff

Development and validation of an MRI-based method for 3D particle concentration measurement

Daniel D. Borup*, Christopher J. Elkins, John K. Eaton

Department of Mechanical Engineering, Stanford University, 488 Escondido Mall, Building 500, Stanford, CA 94305, USA

ARTICLE INFO

Keywords:
Multiphase flow
Magnetic resonance imaging
Particle-laden flow
Experimental techniques

ABSTRACT

A novel method, denoted MRP (short for Magnetic Resonance Particle concentration), was developed to obtain 3D volume fraction measurements for a dispersed particulate phase in turbulent water flows using Magnetic Resonance Imaging (MRI). MRI images taken near a single stainless steel particle suspended in agarose gel showed good agreement with the analytical solution for the disturbance to a uniform magnetic field induced by an immersed sphere. For a random distribution of particles, a linear relationship between the MRI signal decay rate (R_2^*) and particle volume fraction (ϕ_v) has previously been predicted in the MRI literature. This relationship was investigated for various types of particles suspended in agarose gel vials. Good agreement with theory was observed for particles with a high magnetic susceptibility difference from water. R_2^* was also measured in a square channel flow containing a uniform distribution of titanium particles at two fully turbulent Reynolds numbers. Experimental results again agreed well with theory in the majority of the channel for both Reynolds numbers studied. Data from this flow were used to examine the expected SNR and dynamic range for MRP in future experiments. Some discrepancy was observed near the entry region of the channel, with possible explanations including inflowing fluid and large-scale flow structure effects behind the channel's mixing pin array. Finally, the new method was used to measure the 3D concentration distribution for a streak of titanium particles injected into a turbulent square channel flow with angled ribs. The transport of the streak was analyzed quantitatively, and a minor asymmetry in the channel geometry was shown to have important implications for the mean transport of the particle streak.

1. Introduction

1.1. Background

Turbulent, dispersed multiphase flows occur across a wealth of applications, from complex engineered systems to biological and environmental flows. Canonical examples from the engineering arena include the behavior of particulate matter ingested into gas turbine engines (Dunn et al., 1987), particle suspension and dispersion in fluidized bed reactors (Berruti et al., 1995), or process flows that may contain liquid, solid, and/or gas phases (Sinnott et al., 2011). In the medical arena, particulate transport (either medicinal or noxious) is of critical importance in the human airway system (Kleinstreuer and Zhang, 2010) and the intestinal tract (Sinnott et al., 2017). Environmental particle-laden flows are found in volcanic eruptions (Mastin et al., 2009), coastal sedimentary environments (Papanicolaou et al., 2008), and dust storms (Griffin et al., 2001).

Dispersed multiphase flow prediction requires several interdependent models, with the foundation being a method to predict turbulent flow of the carrier phase in realistic geometries. Computer codes used in engineering design cycles typically solve the Reynolds-Averaged Navier Stokes (RANS) equations for the carrier phase mean velocity field, with a separate model for the particle motion and, in some cases, a third model to compute back effects of the particles on the carrier phase. The addition of particles introduces a myriad of new physical processes that must be either resolved, modeled, or neglected. At an absolute minimum, the drag force of the fluid on the particulate phase is required to determine the particles' motion and resulting concentration distribution. In systems with high mass loading, additional coupling terms are required to accommodate the particle-to-fluid forces and particle-particle collisions. But these momentum transfer terms are still only the tip of the iceberg; particle agglomeration, deposition and erosion along walls, gravitational settling, electromagnetic forces, chemical exchange, and heat transfer may play significant roles in determining particle motion. In the case of volcanic plumes, for example, nearly all of these processes play a key role.

There is a severe lack of experimental data sets for quantitative comparison and validation of multiphase flow simulations in complex

* Corresponding author.
E-mail address: borup@stanford.edu (D.D. Borup).

https://doi.org/10.1016/j.ijheatfluidflow.2018.04.006
Received 31 October 2017; Received in revised form 6 March 2018; Accepted 10 April 2018
Available online 27 April 2018
0142-727X/

geometries. As an example, consider the study of Singh et al. (2014), who used Large-Eddy Simulation (LES) to simulate particle-laden flow through a two-passage ribbed square channel of relevance to the gas turbine industry. Wall impact statistics from the LES were used to identify impact-prone regions and to suggest design improvements, which could easily be implemented by engine designers. Complementary experimental measurements were carried out in the same flow by using adhesive tape to visualize regions of high particle deposition. This facilitated a qualitative comparison to the LES, but little insight was available as to how predictions could be improved. As the authors note in their final conclusion, improved experimental capabilities are needed.

At minimum, a viable validation data set should combine well-understood inflow conditions with robust and quantitative particle phase data. 3D data sets are more useful than pointwise or planar data for understanding complex multiphase phenomena. Pointwise particle measurements can be obtained for some geometries using probes. Akilli et al. (2001), for example, used a fiber optic probe to measure particle concentration and velocity in a turbulent round pipe flow downstream of a 90-degree bend. The experimental data consisted of one-dimensional traces at ten streamwise locations for a total of around 200 data points, a fairly typical number for probe data. So, while the geometry may be somewhat complex, the amount of data is limited when probes are used.

Planar data increases spatial coverage at the cost of limitations on the geometric complexity of the flow that can be studied; most planar techniques make use of a planar laser sheet with a camera oriented at 90° to the sheet, and thus require undistorted optical access from two perpendicular planes. For many application-relevant geometries this requirement can be prohibitive, but for simpler building block flows, particle concentration and 2D velocity can be obtained using well-established techniques such as Particle Image Velocimetry (PIV) and Particle Tracking Velocimetry (PTV). More recent experimental advances include the use of stereoscopic or tomographic imaging configurations (Scarano, 2012), defocused images (Willert and Gharib, 1992), and digital holography (Pan and Meng, 2003); Stereo-PIV can provide three-component, two-dimensional (3C-2D) data, while the other techniques provide three-component velocity in three dimensions (3C-3D).

Multi-camera PIV was recently applied by Liu and Kiger (2016) to make improved, simultaneous concentration and 3-component velocity measurements for a dispersed phase at volume fractions approaching 1%. Their method makes use of a thin light sheet and three cameras; particle locations are identified based on the correlations between images from the three cameras, which provides improved resistance to light blocked between the imaging plane and camera at higher volume loadings. However, this setup maintains most of the traditional limitations of optical techniques. Undistorted optical access is required from *four* planes (the three cameras plus light source). In addition, measurements in flow were only made in one thin 2D plane, although the authors suggest that 3D capability could be feasible by scanning across a volume at high speed.

Planar Laser Nephelometry has also been used to study denser suspensions where resolving individual particles is prohibited. This technique also employs a laser-camera pair, but individual particles are not resolved. Instead, the intensity of the Mie-scattered light is measured by the camera and used to infer the volume fraction over larger regions of the flow. The technique was first presented by Kalt and Birzer (2005), with later corrections to account for attenuation and scattering of the light source introduced in Kalt et al. (2007) and Kalt and Nathan (2007). These validation papers studied concentrations up to 0.01% by volume, while more recent work has provided quantitative data for local volume fractions just below 0.1% (Lau and Nathan, 2016). Once again, the use of a laser and camera requires undistorted optical access, a significant restriction for application-relevant geometries.

1.2. Magnetic resonance imaging

Magnetic Resonance Imaging (MRI) is a widespread technology that is finding increasing application to fluid mechanics problems. MRI-based techniques have a significant advantage over both probe-based and planar laser measurements: 3D data can be obtained without the need for any optical access. A typical data set comprises millions of data points on a regular Cartesian grid with 0.6-mm resolution. The achievable resolution varies depending on geometry, flow, and other parameters and may be better or worse than 0.6 mm. Current capabilities include mean 3-component velocity (Elkins and Alley, 2007), passive scalar concentration (Benson et al., 2010), and temperature (Spirnak et al., 2016) measurements in turbulent flows. The majority of MRI-based techniques provide time-averaged data, although phase-averaged measurements in periodic flows and 2D time-resolved measurements are also possible. MRI has been used to provide 3D measurements inside a wide range of geometrically complex flows including a coral colony (Chang et al., 2009), a double-inlet swirl generator (Grundmann et al., 2012), porous fins (Coletti et al., 2014b), a vacuum cleaner nozzle and cut-pile carpet (Lee et al., 2015), a patient-specific human airway model (Banko et al., 2015), and a rotating vertical-axis wind turbine (Ryan et al., 2016).

1.3. Objectives

The motivation for the present work is to extend the suite of available MRI diagnostics to include measurement of the mean particle concentration distribution in turbulent flows. This protocol will be known as Magnetic Resonance Particle concentration—MRP, for short. A pilot study was undertaken by Coletti et al. (2014a) in which a high-concentration streak of glass microspheres was injected into a round turbulent pipe flow with a 180-degree bend. It was observed that the MRI signal dropped by up to 90% in the core of the streak, which contained 20% particles by volume. The proof of concept study was limited to a qualitative visualization of the particle streak, while the end goal is a fully quantitative, well-validated technique suitable for application-relevant studies. The goals of this work were to identify the physical processes governing the MRP method, perform validation experiments both with and without flow, and demonstrate the ability to measure the 3D particle concentration distribution quantitatively in a turbulent flow relevant to gas turbine cooling systems.

2. Theoretical framework

Magnetic Resonance Imaging makes use of the tendency for charged atomic nuclei (e.g., the proton nucleus of a hydrogen atom) to precess around an applied magnetic field. The rate of precession is known as the Larmor frequency and is governed by the magnetic field strength, B_0, and a parameter known as the gyromagnetic ratio, γ, according to the relationship:

$$\omega_0 = \gamma B_0 \tag{1}$$

Typical full body medical MRI scanners use 1.5 or 3 T primary magnets.

Imaging is carried out by sequentially acquiring data points in spatial wavenumber space, i.e., discrete samples of the 3D Fourier Transform (3DFT) of the physical signal. This process occurs as follows. First, a radio frequency (RF) excitation pulse is used to rotate the protons, initially aligned with the B_0 field, into the transverse plane. The protons immediately begin to precess at the Larmor frequency, but can be considered stationary and in-phase in a reference frame rotating at ω_0. Next, linear magnetic field gradients are applied in the three Cartesian directions to vary the local resonance frequency across the sample. By controlling the gradient amplitude and duration, different degrees of phase accumulation can be achieved in each direction. This is the physical analogue of multiplication by a complex exponential basis function in the Fourier transform, where the wavenumber is

determined by the gradient area. The rotating spins induce an electromagnetic response in the coil surrounding the sample, so that each measurement taken is effectively the integral of the complex-valued signal over the entire volume. Once all of wavenumber space has been filled in this manner, an Inverse Fourier Transform returns the physical space data.

Since the density of hydrogen protons is constant, the local amplitude of the MRI signal should remain constant in time according to this idealized description. However, thermal motion of the molecules and other perturbations to the magnetic field will cause the signal magnitude, $s(t)$, to decay exponentially according to Eq. (2):

$$s(\mathrm{TE}) \propto \mathrm{e}^{-R_2^* \times \mathrm{TE}} \tag{2}$$

where the signal decay rate is denoted R_2^* ("R Two Star") in a Gradient-Recalled Echo sequence (GRE) and TE is a user-controlled parameter known as the "echo time" that sets the delay between RF excitation and signal acquisition. Note that R_2^* has dimensions of inverse time; the use of frequency units is discouraged here to avoid confusion with the many oscillatory processes at work in an MRI experiment.

Small paramagnetic or diamagnetic microparticles dispersed in water increase the signal decay rate by locally disturbing the magnetic field. Yablonskiy and Haacke (1994) considered this effect in the so called "static dephasing" regime, which refers to a size range of objects for which the water self-diffusion length scale is much smaller than the object size. In the presence of randomly distributed spheres, R_2^* is increased by the following additive factor, adapted from Eq. (11) of Yablonskiy and Haacke (1994):

$$R_{2,part}^* = A\phi_v = \frac{8\pi^2}{9\sqrt{3}}\gamma B_0 |\Delta\chi|\phi_v \tag{3}$$

where A is a convenient symbol that will be referred to as the "calibration constant" and $\Delta\chi$ is the dimensionless magnetic susceptibility difference between the particle and surrounding fluid expressed in Electromagnetic Units (EMU). A, like $R_{2,part}^*$, takes on units of inverse time—values of the calibration constant can be thought of as 1/e decays per time per unit ϕ_v. For water, $\chi = 0.720 \times 10^{-6}$—this and all further susceptibility values are taken from Schenck (1996), which reports values in SI. Eq. (3) predicts that imaging at higher field strengths and/or using particles with a larger susceptibility difference from water will boost the signal decay at low concentrations, and, notably, shows no dependence on diameter.

The linear relationship between $R_{2,part}^*$ and ϕ_v forms the basis of MRP. Relatively few studies have been carried out to quantify the precise concentration of a dispersed phase using R_2^*, as described here. Girard et al. (2012) and Kuhlpeter et al. (2007) observed a highly linear relationship between R_2^* and iron oxide nanoparticle (IONP) concentration in samples containing human cells; sensitivity to the location of the IONPs (internal or external to the cells) was observed, but this issue is not present in a turbulent flow and did not affect linearity of the relationship in either case. Dixon et al. (2009) used changes in signal to the surrounding tissue to estimate IONP quantities by fitting point dipole models to the data, while Robson and Hall (2005) used a similar process to differentiate between particles of different material composition. These approaches differ from measurement of R_2^*, and would not be suitable for a flowing system, but both demonstrate the underlying physics of a single particle, or localized agglomeration.

The effect of a single spherical particle on the local signal has been solved analytically. The following formulation was adapted from the solution for field disturbance around a sphere presented in Yablonskiy and Haacke (1994). Any point in the fluid can be described by its position relative to the particle center. In polar coordinates this is expressed as (r, θ, ϕ), where θ describes the polar angle from the direction of the B_0 field. Using these coordinates we can define a dimensionless "dephasing position" u_p:

$$u_p(r, \theta, \phi) = \frac{\rho(r, \theta, \phi)}{d_p}\left[\frac{2}{3}\gamma B_0(\Delta\chi)(TE)\right]^{-1/3} \tag{4}$$

where d_p is the particle diameter and ρ is an "equivalent polar radius" that accounts for the shape of the field disturbance function:

$$\rho(r, \theta, \phi) = r\left[\frac{3\cos^2(\theta) - 1}{2}\right]^{-1/3} \tag{5}$$

Note that $\rho = r$ at $\theta = 0$ and π. The local signal magnitude S (normalized by its undisturbed value S_0) can then be defined in terms of u_p alone:

$$\frac{S}{S_0} = \exp\left[\frac{-i\pi}{2u_p^3}\right] \tag{6}$$

This is simply a phase shift of $-1/2u_p^3$ radians in the complex plane. A large amount of phase change within a measurement voxel produces signal loss, so Eq. (6) can be used to predict the spatial extent of the particle's effect on the signal. Since u_p can become negative (for $\Delta\chi < 0$ or θ near 90 °), the phase shift can occur in either direction, but this distinction is unimportant for signal magnitude; the real component of S/S_0, which always returns to unity for sufficiently large $|u_p|$, may be considered a proxy for signal loss. For example, there is less than 50% drop in $\mathrm{Re}(S/S_0)$ at any point where $|u_p| > 1.15$, and less than 10% drop for $|u_p| > 1.52$. By examining Eqs. (4) and (5), we see that a given u_p corresponds to increasing r as either TE or $|\Delta\chi|$ is increased. In other words, longer echo times or particles of higher magnetic susceptibility will produce significant signal decay across a larger physical region. Eq. (5) also shows that, for a given u_p, the largest r corresponds to $\theta = 0$ or π, i.e., the signal decay will extend farthest along the B_0 field axis. This distance is only 20% smaller in the equatorial plane ($\theta = \pi/2$) but, notably, drops to zero at around 55° from the B_0 axis.

Turbulent flow is the source of a number of artifacts in MRI data. The primary change of interest here is a decrease in undisturbed magnitude, S_0, in regions of strong turbulence. The primary mechanism for this is a process known as "turbulent dephasing." Turbulent velocity fluctuations during a scan produce noise in the raw, Fourier-space data. When the inverse Fourier transform is taken during reconstruction, each bit of noise is interpreted as additional signal at some unpredictable location in the measurement domain. The result is a decrease in S_0 within the turbulent region, and a corresponding increase in noise as the signal is spread across planes of data containing the turbulence. Very high turbulence levels, such as those found downstream of a stenosis, can cause complete signal loss (Oshinski et al., 1995). A technique called "flow compensation," present in many MRI sequences, can often mitigate this effect to some degree. The reader is directed to Fong (2005) for a comprehensive overview of additional flow-related artifacts that may occur in MRI.

3. Preliminary static experiments

For all experiments described in this paper, a 3 T medical-grade MRI machine was used (GE Healthcare). Imaging was performed using an RF-spoiled GRE sequence, with the following scan parameters employed across all experiments, unless otherwise noted: 20° (flow calibration only) or 30 ° flip angle; 62.5 kHz readout bandwidth; 10 ms TR; and exclusion of the "corners" of k-space for 3D imaging. Water containing dissolved copper sulfate ($CuSO_4$) was used as the base fluid for gel suspensions and the working fluid for all flowing experiments. The concentration of copper sulfate must be chosen carefully to balance two competing effects. First, higher $CuSO_4$ concentrations (up to a point) produce a larger baseline signal value due to a process known as spin-lattice relaxation, which occurs more rapidly at higher molarity. Higher signal values typically lead to a higher measurement signal-to-noise ratio (SNR), which allows for improved resolution in decay rate (and, thus, ϕ_v). In velocity measurements, where TE is made as short as

possible, the baseline signal is the dominant issue, so a fairly high concentration of 0.06 M is typically used.

The second effect is that R_2^* of the solution increases with $CuSO_4$ concentration. This background decay rate *adds* to the particle-induced decay rate, so that total signal loss at a long TE will occur at lower particle volume fractions. Total signal loss at a given TE is undesirable, as the signal no longer depends on the exact R_2^*. Thus, increasing the $CuSO_4$ concentration decreases the dynamic range of the measurement in terms of the highest resolvable ϕ_v. A concentration of 0.01 M was chosen for MRP to balance these competing effects. Signal loss at a TE of 7.5 ms for the 0.01 M solution, for example, is around 10%. The use of different $CuSO_4$ molarities is not explored here, but could be pursued in future work. The magnetic susceptibility of 0.01 M copper sulfate solution is within 2% that of pure water: $\chi = 0.706 \times 10^{-6}$ (Schenck, 1996). For brevity and clarity, otherwise clean (i.e., no particles) copper sulfate solution is hereafter referred to as "working fluid" or simply "fluid."

Several sets of gel suspensions were prepared by stirring agarose powder (ThermoFischer Scientific) into working fluid that had been brought to a boil. The agarose comprised 2% by mass of the final gel. Immediately after the agarose powder dissolved fully, a known amount of the solution was poured into a small container in preparation for adding particles.

3.1. Single particle

A 30-mL glass vial was prepared containing a single 105-μm diameter stainless steel microsphere (type 304, LPW Technologies). Preparation was carried out by first placing the lower half of the vial into an ice bath until the liquid agar solidified. The particle was identified from a powder sample, measured with a jeweler's microscope, picked up by electrostatic adhesion to a needle, and released into the vial where it settled to the surface of the congealed section. After the remainder of the agar gel was allowed to cool, the location of the particle was identified and marked on the vial exterior to aid in imaging.

For the single-particle gel, signal was obtained at a single echo time of 10 ms on an isotropic, 1 mm^3 grid. Fig. 1a shows the signal magnitude in the vicinity of the 105-μm stainless steel particle. Three planes of data surrounding the particle are shown, with the particle located in the center voxel of the middle plane. The B_0 direction is toward the top of each plane. Although the particle was much smaller than a voxel (only 0.06% by volume), over 50% signal reduction is observed in the central voxel. Significant signal reduction is also visible in all six immediately adjacent voxels (i.e., voxels left, right, above, and below center in the middle plane, and center voxels in the left/right planes). The dephasing position $u_p = 1.15$ corresponds to a polar radius $\rho = 1.4$ mm for this experiment, a prediction that aligns well with the roughly 3-voxel extent of signal decay observed.

To more thoroughly assess the accuracy of the theory, Eqs. (4)–(6) were used to simulate the signal near a 105-μm diameter particle on a 0.05-mm isotropic grid. The results were averaged onto a 1 mm^3 grid for comparison with the MRI data. Particle position and susceptibility were allowed to vary until the closest fit to the data was obtained. Good agreement is found between the simulated signal in Fig. 1b and the experimental data. The simulation is also reported on the 0.05-mm grid in Fig. 1c to show the shape of the decay region. The best fit was obtained for a particle susceptibility $\chi = 315 \times 10^{-6}$, well within the range of reasonable values for nonmagnetic stainless steel reported in Schenck (1996).

It is clear from these results that certain particles can induce marked signal decay across a handful of neighboring voxels. This effect would result in smoothing of the actual concentration field for an experiment with unknown particle distribution. However, Eqs. (4)–(6) accurately predict the spatial extent of signal loss for a given choice of particle and imaging parameters. These equations should be used when designing an experiment to minimize bleeding of the signal loss between neighboring voxels.

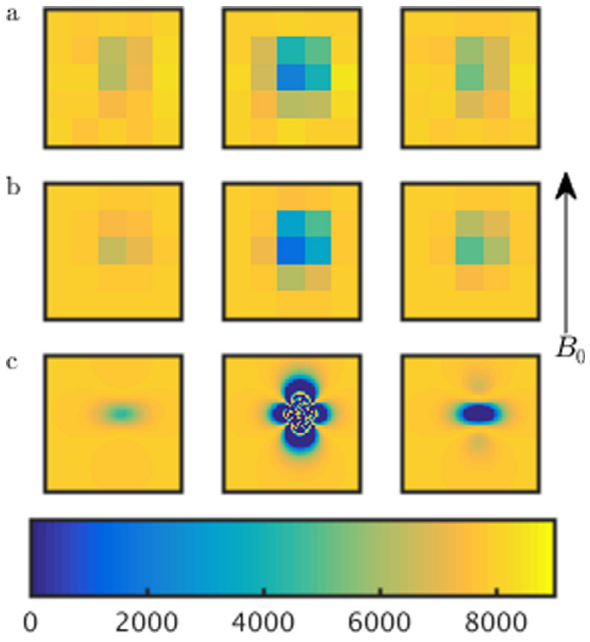

Fig. 1. Color contours of MRI signal magnitude at TE = 10 ms for a single particle in agarose gel. (a) Three adjacent planes of the 3D data set are shown from L-R in the top row, where a 105-μm stainless steel particle was located in the center voxel of the middle plane. The B_0 direction is indicated at right. (b) Signal decay was simulated using Eqs. (4)–(6) to assess the accuracy of the theory. (c) The simulated signal is also reported on a 20x finer mesh to show the shape of the decay region. Magnitude units are arbitrary.

3.2. Homogeneous gel suspensions

Homogeneous suspensions were prepared by adding a known mass of particles to the liquid agarose solution and agitating by repeated inversion to maintain a uniform particle distribution. Agitation was halted just before the gel congealed to allow some time for air bubbles to escape. A small amount of particle settling occurred during this congealing time, which led to a region of high concentration at the bottom and low concentration at the top of each sample. These regions were less than 5% of the sample container height, and were excluded from processing. The settling process was not expected to affect the mean concentration in the sample center, as each particle settled approximately the same distance during the final congeal time.

Titanium particle suspensions were prepared in 30 mL glass vials. The titanium particles were grade 23 titanium alloy (density $\rho = 4430$ kg/m^3) obtained from LPW Technologies. The nominal diameter of these particles reported by the manufacturer was 15–45 μm. Gu et al. (2014) examined a similar titanium powder from LPW and found a Mean Volume Diameter (MVD) of 33 μm using laser diffraction, with a standard deviation of 9 μm. Examination of 30 randomly-selected particles using a jeweler's microscope yielded particle sizes comparing favorably to the manufacturer specifications and the literature-reported MVD. Additional suspensions of 50 μm glass microspheres (Potters Industries) and -200 mesh (<75μm) bismuth and graphite powders (ThermoFischer Scientific) were prepared in 100-mL plastic jars to investigate the effects of particle material.

The homogeneous gels were imaged at a variety of echo times as the technique was being developed during these experiments. Pointwise signal decay rates were computed by simple linear regression after the natural logarithm of the mean signal was computed. Background subtraction was not available since the particle positions were fixed, so only the total R_2^* could be obtained. The measurement resolution was

Table 1
Measured and predicted calibration constants for four particle materials. Susceptibility values taken from Schenck (1996).

Material	ϕ_v (%)	χ (EMU) $\times 10^6$	A (ms^{-1}) Pred.	Meas.	R^2
Glass	0 – 4	−1.10	1.6	3.5	0.997
Bismuth	0 – 0.34	−13.1	50	42	0.977
Graphite	0 – 0.29	−16.2	63	63	0.987
Titanium	0 – 0.46	+14.5	62	64	0.990

between 0.8 mm and 1 mm for all gel experiments and the results were spatially averaged over the central portion of each vial.

Table 1 lists relevant experimental parameters and results for each of the gel particle suspensions. The range of ϕ_v studied was chosen a priori so that R_2^* values would be in approximately the same range for each material. The predicted values for the calibration constant, A, were obtained using Eq. (3), while measured values were obtained by linear regression on the mean R_2^* versus ϕ_v curves for each sample. The agreement between data and theory is very good for the titanium and graphite, fair for the bismuth particles, and relatively poor for glass. The high-susceptibility particles have the additional benefit of providing high contrast at volume fractions well below 1%, making them more suitable for the study of dilute flows.

The titanium particles were chosen for subsequent experiments because of their relatively low cost and high degree of sphericity. One can compute that for a titanium particle with $d_p = 50\,\mu$m, scanned at TE = 7.5 ms, the dephasing radius $u_p = 1.15$ corresponds to less than 0.25 mm at any angle. Since the great majority of particles in the titanium sample are smaller than 50 μm in diameter, imaging at typical MRI resolutions down to around 0.6 mm is reasonable.

Glass—or other similar particles—may still be useful to the study of slurry, sedimentary, or other high-concentration flows. However, processes beyond the susceptibility-induced magnetic field disturbance appear to play a significant role in enhancing signal decay near these weakly magnetized materials. Additional study would be needed to support the calibration in the small-$\Delta\chi$ regime, as a simple linear model might no longer apply or other parameters might not vanish. For example, effects confined to the particle-fluid interface could scale with diameter rather than susceptibility; this would cause obvious difficulties in studies with a polydisperse particle phase.

4. Turbulent flow calibration

4.1. Experimental configuration

Calibration measurements were obtained in a square channel flow with a homogeneous distribution of particles. The main flow was supplied by a 1/3 horsepower centrifugal pump (Little Giant #TE-5.5-MD-HC), controlled via a gate valve, and monitored with a paddlewheel flowmeter (Blue-White Industries). All other flows were supplied by Little Giant centrifugal or submersible pumps, controlled with needle valves, and monitored using an ultrasonic flowmeter (Transonic Systems). The same titanium particles from the gel suspension study were used for all flowing particle experiments.

An MRI-compatible particle feed system was constructed to provide the continuous supply of particle-laden working fluid at a known particle concentration. This apparatus consisted of a large acrylic cylinder containing the particle-laden fluid that could be rotated constantly to keep the particles suspended. A rubber bellows partitioned the cylinder into two compartments. The interior of the bellows was then filled with fluid at a known rate to displace an identical quantity of particle solution into the experimental flow without diluting the particle mixture. The feed system is described in further detail in Borup et al. (2017). The working fluid was recirculated during a scan, requiring particle removal after the flow passed through the test section. Particle-laden fluid exiting the apparatus was directed to a settling tank, where most of the particles fell to the bottom, before being pumped back to the supply tank through two 0.5 μm filters.

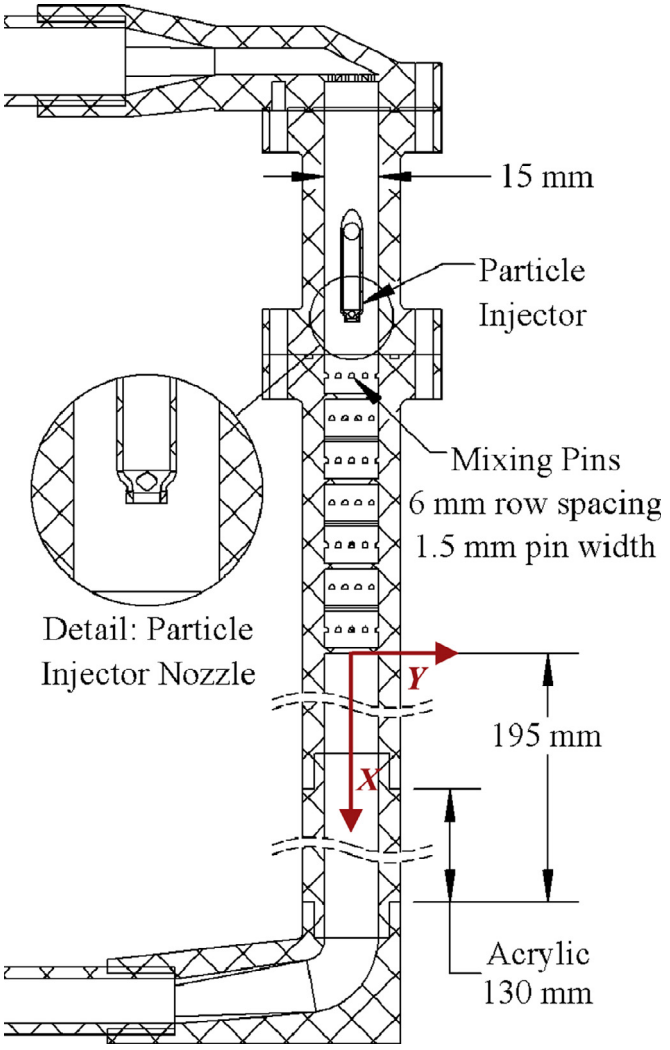

Fig. 2. Schematic (cut section view) of the calibration channel showing 90-degree inlet bend, particle injector, mixing pins, and square channel calibration region. Inset detail shows the nozzle-shaped injector with side-cuts to promote mixing of the particle stream.

The calibration channel was designed to achieve a uniformly-distributed mixture of particles in a 15-mm wide square channel flow. A cut section of the channel is shown in Fig. 2. A vertical orientation of the flow was chosen, despite the restricted vertical clearance in the MRI scanner (Fig. 3), to ensure that gravitational settling did not cause particles to concentrate on one side. For all cases, 80% of the total flow (the "main" flow) was working fluid supplied through the upper passage of the channel. The remaining 20% was injected via the shaped nozzle visible in the inset detail of Fig. 2. Two fully turbulent Reynolds numbers were studied: 6300 and 12,200, based on the square channel width and the bulk velocity after particle injection. The flow was not assumed to be fully developed because of the short development length available inside the MRI bore; however, in a fully developed channel, the slow and fast cases would correspond to $Re_\tau = 205$ and 364, respectively.

The velocity ratio of the streak (V_{streak}/V_{main}) was set to approximately 3, so that vigorous turbulent mixing was expected immediately upon injection. The flow then proceeded through 14 rows of 1.5-mm diameter pin fins, staggered and alternating in orientation, which

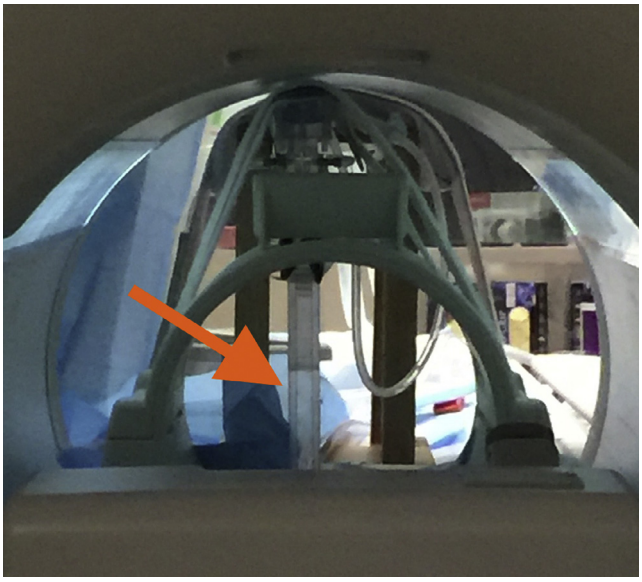

Fig. 3. The calibration channel was designed to generate a homogeneous particle distribution in the short vertical space of the MRI scanner. An orange arrow identifies the intended calibration region.

spread the particle streak across the entire channel while diffusing the streak momentum. The feeder supplied particles at 4% by volume so that the maximum achievable concentration after mixing was approximately 0.8%; variation in the particle concentration was achieved by slowing the feeder flow and diluting the concentration of the streak before injection into the channel. A Labview script continuously read in all of the flowmeter measurements via an NI-DAQ device; these values were converted to a readout of ϕ_v that was used in real-time to set and monitor the concentration for each case. The exact uncertainty in mean ϕ_v varied from case to case, but was generally between 0.02% and 0.01%. MRI data were acquired across the entire channel from the second-to-last row of pins to just upstream of the channel exit bend.

In analyzing the results for the experiments with flow, it will often be useful to consider the Stokes number, a dimensionless parameter that describes the tendency for particles to follow the flow streamlines. A Stokes number much smaller than 1 indicates particles that act as flow tracers, while a Stokes number much larger than 1 indicates no sensitivity to the surrounding flow. The Stokes number is defined as:

$$\mathrm{Stk} \equiv \psi\frac{\tau_p}{\tau_f} = \psi\frac{\rho_p d_p^2 U}{18\mu_f H} \tag{7}$$

where τ_p is the particle aerodynamic time constant, ρ_p and d_p are the particle density and diameter, μ_f is the fluid dynamic viscosity, and $\tau_f = H/U$ is a fluid time scale based on an appropriate length, H, and velocity, U, from the flow. ψ is a correction factor important in cases where the particle Reynolds number, $\mathrm{Re_p}$ (based on the same U and d_p), is O(1) or greater. The titanium particles used in this experiment, at the mean diameter, have $\tau_p = 0.268$ ms in 20 °C water.

4.2. Results

An outline of the MRP processing scheme is presented in Fig. 4. MRI signal was obtained at three TEs: 2.5, 5, and 7.5 ms. The measurement resolution was 1.0 × 0.8 × 0.8 mm in the *X, Y, Z* directions, respectively. Readout was performed in the *X* direction. Multiple scans with and without particles were performed and averaged together to improve SNR: 6 scans per particle case and 20 scans per no-particle case. Signal decay was calculated using the "fit" function from the MATLAB Curve Fitting Toolbox (MathWorks, Inc.). This function employed a weighted, nonlinear least squares method to optimize the fit of an exponential model with two parameters: initial signal magnitude and decay rate. The weight used for each data point in the fitting routine was the inverse of its 95% confidence interval, which was computed from the scan-to-scan variation in signal magnitude according to Eq. (8):

$$95\%\text{C. I.} = \pm\frac{\hat{\sigma}(S)\, t_{n,.025}}{\sqrt{N}} \tag{8}$$

where N is the number of scans, $n = N - 1$, $\hat{\sigma}(S)$ is the measured standard deviation of the signal, and $t_{n,\alpha}$ is the Student t distribution (Bendat and Piersol, 2011).

The baseline magnitude and decay rate in each voxel were computed for the no-particle case data first, as this data had the highest SNR. For each Reynolds number, initial magnitudes from the no-particle case were prescribed in the fitting algorithm for the particle cases, which had lower SNR, to limit overfitting error. The particle contribution to the signal decay rate ($R^*_{2,part}$, from Eq. (3)) was then taken to be the difference between particle and no-particle case R_2^* values at each spatial point.

The theory of Yablonskiy and Haacke (1994) is limited to a monodisperse, randomly distributed particle phase with no motion relative to the surrounding fluid. Molecular diffusion in the fluid over the relevant time scale (i.e., TE) is assumed to occur on length scales much smaller than the particle size. It was not readily apparent, then, whether this theory would accurately describe the signal decay for a turbulent, dispersed multiphase flow; one could imagine errors arising from the particles' preferential concentration by turbulence or, more generally, from their highly variable position and velocity distribution. However, the majority of data obtained in the calibration rig suggest that the unsteadiness manifests primarily as measurement noise rather than bias.

The primary region of interest (ROI) used to investigate the $R^*_{2,part}$ vs. ϕ_v calibration was a rectangular prism, 21 voxels in streamwise extent and 8 × 8 voxels in cross-section. One plane of the ROI is shown in Fig. 5a. The remainder of the figure shows $R^*_{2,part}$ in the same plane of the ROI for the seven cases studied. The color map is held constant across cases at each Reynolds number, permitting a qualitative assessment of the signal-to-noise ratio as well as the general effect of changing particle concentration. Due to the limited number of scans per case, the noise level is higher than would be expected for a full-scale experiment, but the homogeneous particle distribution allows for noise reduction by averaging over the full ROI.

Fig. 6 shows the signal decay rate data, averaged over the ROI, versus the bulk volume fraction. All cases are reported in the main figure, while the inset is focused on the lower-concentration, high Reynolds number data points. The mean calibration constant measured was 65 $\mathrm{ms^{-1}}$ for the low-Re flow and 63 $\mathrm{ms^{-1}}$ for high Re. Both values are within 5% of the theoretical prediction, $A = 61.4$ $\mathrm{ms^{-1}}$, while the variation with Reynolds number change is around 3%. These discrepancies are within the uncertainty expected from imperfect knowledge of bulk ϕ_v (shown as horizontal error bars at each point). The results suggest that A is insensitive to the Reynolds number and follows reliably from Eq. (3). While only two flow conditions were considered, the mean velocities (approximately 0.4 and 0.8 m/s) and turbulence levels at these two flow rates are representative of the majority of MRI-based turbulent flow studies.

An examination of the noise level characteristic of MRP was also carried out in this same ROI, where the actual mean concentration of particles is assumed to be uniform across all voxels. An important quantity in MRI is the "SNR efficiency," defined as:

$$\eta_{\mathrm{SNR}} = \frac{\mathrm{SNR}}{\sqrt{\mathrm{T_{scan}}}} \tag{9}$$

where $\mathrm{T_{scan}}$ is the total scan time. In MRI, SNR generally increases proportionally with the voxel volume and the square root of the total scan time (Parker and Gullberg, 1990). SNR efficiency is thus useful for

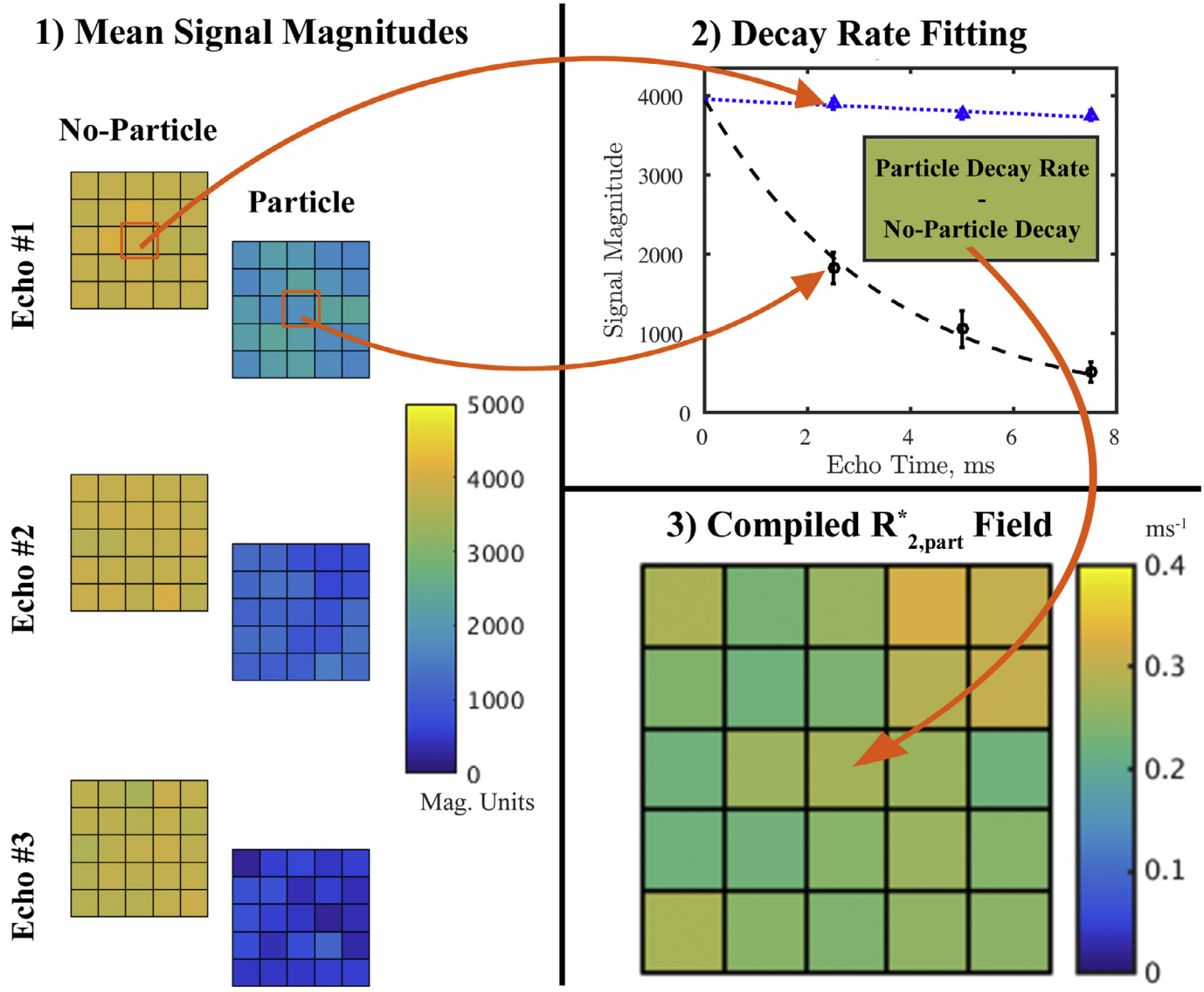

Fig. 4. MRP processing diagram for a sample 5 × 5 plane of data in a turbulent flow. 1) Signal is acquired at multiple echoes, both with and without particles, and averaged across many scans. 2) For each voxel, a decay rate curve is fit to the particle and no-particle data, where the initial amplitude determined from the no-particle curve is enforced in fitting the particle data. 3) The 3D $R^*_{2,\mathrm{part}}$ map is compiled from the difference between particle and no-particle decay rates in each voxel. Data shown are from the turbulent flow calibration, where confidence intervals in step 2 have been scaled to their expected level for a full-length experiment.

estimating the achievable SNR because the available scan time can vary significantly from experiment to experiment. The SNR was computed on the 1344-voxel ROI. The signal was defined to be the measured mean decay rate, $\hat{\mu}(R^*_{2,\mathrm{part}})$, while the noise (which followed a roughly Gaussian distribution) was defined as the measured standard deviation, $\hat{\sigma}(R^*_{2,\mathrm{part}})$. 95% confidence intervals on both quantities were small: $\pm\, 0.05\,\hat{\sigma}(R^*_{2,\mathrm{part}})$ for the mean decay, and $\pm\, 0.08\,\hat{\sigma}(R^*_{2,\mathrm{part}})$ for the standard deviation.

Table 2 shows the SNR efficiency for each case studied. Only the time spent acquiring particle-laden scans was considered in determining SNR efficiency. This is because the capacity of the particle feeder places the main restriction on achievable scan time in MRP experiments, which makes the particle-laden data the primary source of noise in $R^*_{2,\mathrm{part}}$. In the present experiment, all seven cases were performed with a single feeder loading. Each case consisted of approximately 2.5 min of data, which led to fairly low SNR. Much longer averaging times should be possible for future experiments where only one or two acquisition cases are considered. Taking a 30-min scan (at the same measurement resolution) as an example, SNR > 18 would be expected for volume fractions from 0.1% to 0.85%, with SNR > 11 achieved even at $\phi_v = 0.05\%$ and Re = 12, 200. A more typical choice of 0.7 mm isotropic voxels would decrease these values to 9.5 and 5.8, respectively, since SNR scales with the voxel volume.

It is also interesting to note that η_{SNR} decreases at both the high and low ends of the ϕ_v range. The drop at low ϕ_v is due to loss of a resolvable change in $R^*_{2,\mathrm{part}}$, while the drop at high concentration occurs due to complete signal loss at the later echoes, as discussed previously. This behavior provides a look at the achievable dynamic range of MRP. The lowest concentration, $\phi_v = 0.05\%$, is a reasonable choice for the smallest resolvable concentration due to the SNR near 5 for a typical scan. Unfortunately, the full roll-off of SNR at high ϕ_v was not captured in this experiment. However, $\phi_v = 0.85\%$ is about as well-resolved as 0.1%, so doubling of this value to $\phi_v \approx 1.5\%$ could serve as a fair estimate of the maximum resolvable concentration, producing a dynamic range of around 30. It should be kept in mind that the achievable dynamic range is sensitive to the flow conditions and scan parameters. For example, a lower baseline signal level exists in regions of high turbulence, so the dynamic range of MRP will be locally decreased in these regions.

Similar values of A were observed throughout the bulk of the channel. However, some discrepancy was observed in the region just

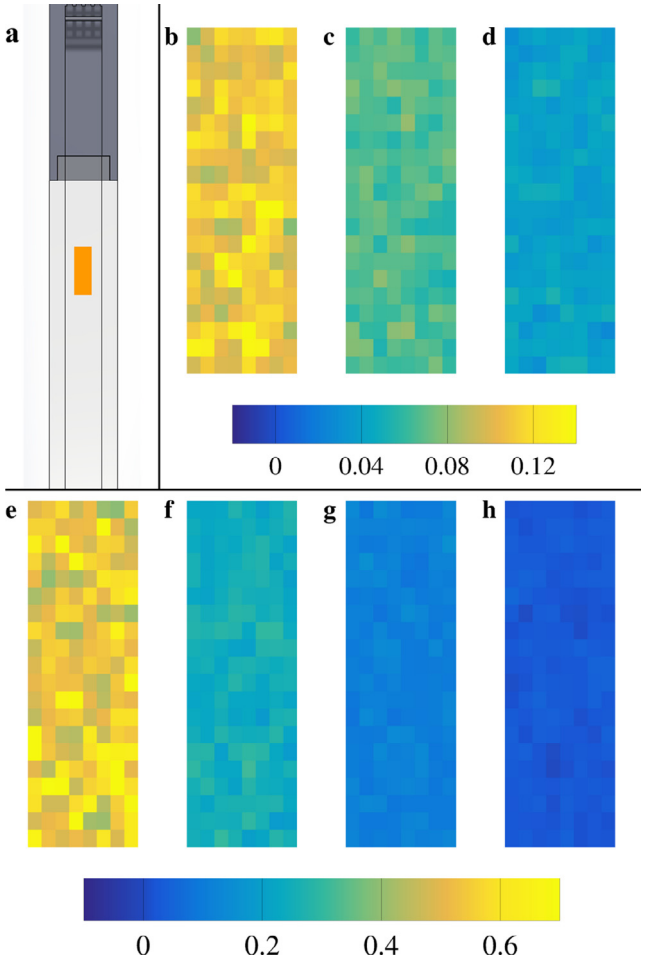

Fig. 5. Particle-induced signal decay rates ($R^*_{2,part}$) measured in the center of the calibration channel. The location of the primary calibration region within the channel is indicated by a small orange rectangle (a). Contours of $R^*_{2,part}$ in a central plane of the ROI are shown for Re = 12, 200 at ϕ_v = 0.19%, 0.11%, and 0.05% (b–d), and for Re = 6, 300 at ϕ_v = 0.85%, 0.42%, 0.21%, and 0.10% (e–g).

Table 2
SNR efficiency for all calibration cases.

Re	Bulk ϕ_v (%)	$\hat{\mu}(R^*_{2,part})$ (ms^{-1})	$\hat{\sigma}(R^*_{2,part})$ (ms^{-1})	η_{SNR} ($min^{-1/2}$)
6300	0.85	0.535	0.082	**4.1**
6300	0.42	0.259	0.029	**5.5**
6300	0.21	0.124	0.0140	**5.5**
6300	0.10	0.047	0.0085	**3.4**
12,200	0.19	0.110	0.0118	**5.8**
12,200	0.11	0.059	0.0083	**4.4**
12,200	0.051	0.022	0.0068	**2.0**

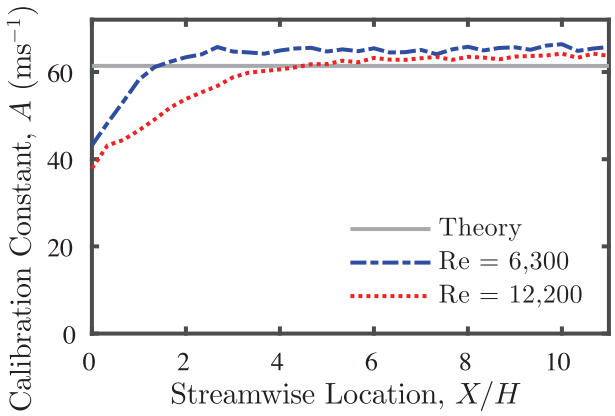

Fig. 7. Dependence of calibration constant, A, on streamwise location in calibration channel. Streamwise locations are normalized by the channel height and refer to distance from the last row of mixing pins.

downstream of the mixing pins, which was more pronounced for the high-Re case. In Fig. 7, the mean A over a sliding 5 × 8 × 8 voxel region is reported as a function of the region's streamwise position in the channel. Discrepancies with theory are observed for $X/H < 2$ at low Re, and $X/H < 4$ for high Re. In assessing the validity of MRP, it is important to explore potential sources for this discrepancy in detail. Any explanation must account for two factors: why the discrepancy was observed only in the channel entry region, and why the high-Re case was disproportionately affected.

The unsteady fluctuation in the particle concentration field is one likely cause. Although $R^*_{2,part}$ itself is a linear function of ϕ_v, the MRI scanner actually measures the signal magnitude, which is a nonlinear

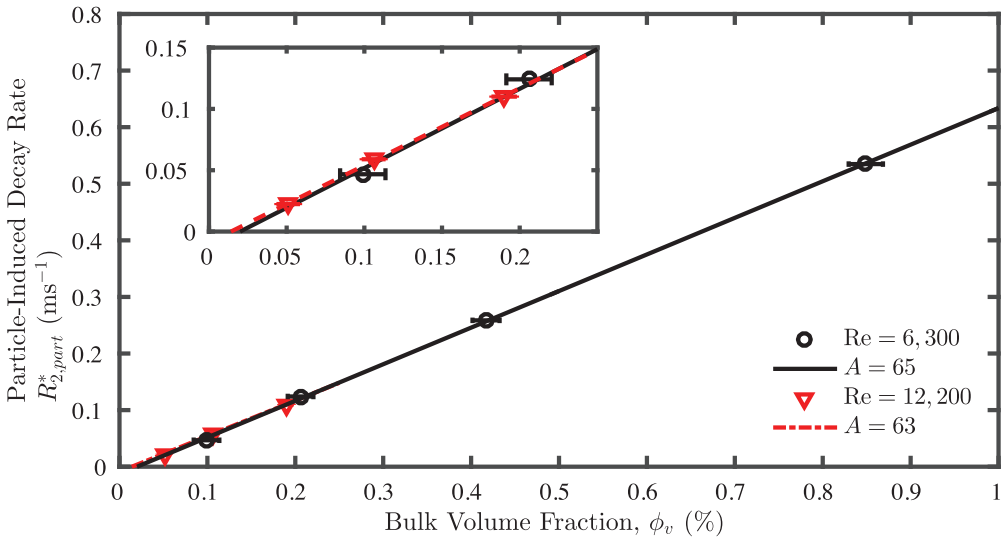

Fig. 6. Calibration curves in channel center. Inset shows detail of calibration at high Reynolds number.

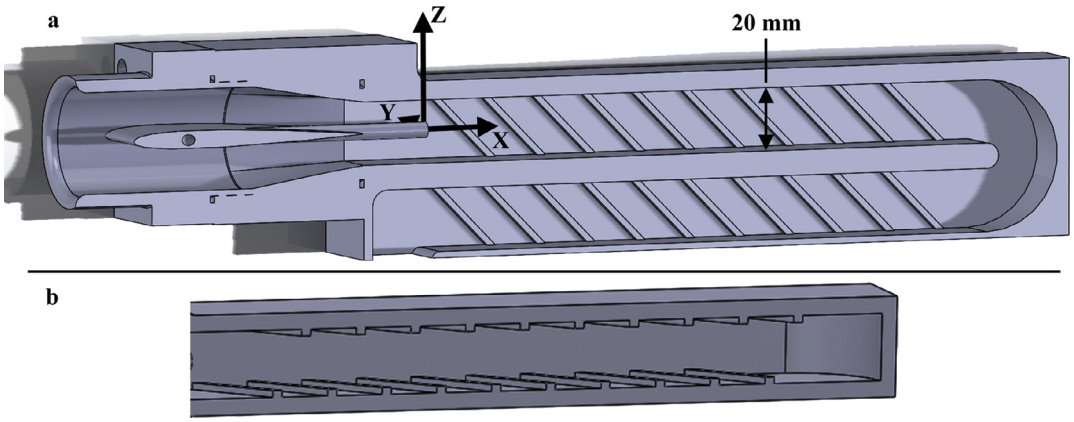

Fig. 8. Rendering of the SGTIP model. The square channel is 20 mm wide, and the ribs are 2 mm tall. (a) A side view with front wall removed shows the particle streak injector at the upper left, one of the two ribbed walls, and the coordinate system centered at the point of injection. (b) A bottom (− Z direction) view of the first passage with the dividing wall removed shows the staggered arrangement and relative height of the ribs.

function of the total R_2^* according to Eq. (2). Therefore, it might be expected that averaging across fluctuations in ϕ_v could produce nonlinearity errors in A. However, particle clustering occurs everywhere in a turbulent flow due to preferential concentration, so unsteadiness alone fails to explain why the discrepancy in A is limited to the channel entry region.

An estimate of the length scales for nonuniform particle concentration structures provides some resolution here, as these scales differ over the length of the channel. Near the channel entry, where the discrepancy in A was observed, wake regions are present behind the upstream mixing pins. Tang et al. (1992) showed that particle clusters in a planar wake will occur over length scales comparable to the wake width, particularly for particle Stokes numbers near unity. For the high-Re flow, using the pin width (1.5 mm) for H and bulk velocity through the inter-pin gaps (1.4 m/s) for U yields Stk = 0.12. Thus, multi-voxel size clusters may reasonably be expected to form, particularly given the polydisperse particle supply and d_p^2 dependence of the Stokes number. Meanwhile, in downstream portions of the channel, where A agreed well with theory, clusters and voids are expected to form due to preferential concentration. The Kolmogorov microscales are most relevant for this process. The bulk flow conditions and channel height were used to estimate the Kolmogorov length scale, $\eta = 13\,\mu$m, and time scale, $\tau_\eta = 0.167$ ms. Eaton and Fessler (1994) showed that particle clusters are expected to form at length scales of 6–20 η when Stk_η is around 1. In this flow, $\mathrm{Stk}_\eta = 1.4$, so that preferential concentration over 80–260 μm scales is expected, well below the voxel size. One possible explanation, then, is that nonuniform particle concentration structures affect the MRP calibration only when the size of these structures equals or exceeds the measurement voxel size.

Another potential explanation for the lower A value in the upstream portion of the channel are so-called "inflow effects," commonly observed in MRI images with flow. The phenomenon occurs because hydrogen protons entering the MRI imaging coil have not yet been exposed to any RF excitation pulses. After several RF pulses (typically between 3 and 10) the protons reach a steady state of magnetization from one pulse to the next. Inflow effects arise in the interval between these two periods; the signal magnitude of inflowing hydrogen may be higher, lower, or phase-shifted compared to the steady-state protons. Data in the inflow region are normally discarded during post-processing for well-established MRI techniques. The inflow length for 5 RF pulses corresponds to about 2 and 4 channel heights for the low and high Re cases, respectively. This is precisely the region over which variations of A were observed in Fig. 7. While the exact mechanism through which a modification to A would occur is not known (the theory does not consider any effect of RF pulses), inflow effects represent a second possible explanation for the discrepancy, and one that can often be avoided by careful design of the experimental geometry.

To provide additional support for the validity of the method, the computed particle mass flux was also considered over the region where A did agree with theory. It was first verified in the laboratory setting that no particles accumulated over time anywhere in the channel under particle-laden flow conditions. This meant that the mean particle mass flux was conserved through any streamwise plane. Three-component, 3D mean velocity data (not shown) were acquired using MRI at both flow rates, with no particles present. The low particle mass loadings used (<5%) were not expected to significantly alter the mean flow from no-particle conditions. The flux of $R_{2,part}^*$ was computed from the combined decay rate and velocity data sets for all seven cases. The standard deviation of $R_{2,part}^*$ flux was below 1.5% of the mean flux for six cases, indicating a high degree of consistency. This is identical to observing consistency in the particle mass flux because of the linear relationship of Eq. (3). At the lowest volume loading ($\phi_v = 0.05$ in the high-Re case), the standard deviation of flux was 3.3% of the mean, indicating that this concentration level is approaching the noise threshold.

5. Ribbed channel streak

5.1. Experimental configuration

The final experiment consisted of the titanium particles injected as a streak along the centerline of a 20-mm wide square channel with 2-mm tall, staggered, 45° ribs on the front and back walls. This geometry, known as the Stanford Generic Turbine Internal Passage (SGTIP), is of relevance to the gas turbine industry as a model for the internal cooling passages found in high-pressure turbine blades and vanes. The SGTIP has been used in numerous studies, and details of the flow can be found in Elkins et al. (2004). A cut section of the geometry is shown in Fig. 8.

The pumps and flow control equipment were similar to those used for the calibration channel flow. The particle feeder supplied 2% particles by volume, which was diluted to produce a streak at $\phi_v = 1\%$. The streak was injected isokinetically (i.e., at a velocity ratio of unity) into the main flow, which had a bulk Reynolds number of 20,000. While gravity was acting in the − Z direction, the mean particle settling velocity of 7 mm/s was negligible compared to the bulk velocity of 1 m/s.

The mean-diameter particles in the ribbed channel flow had a Stokes number of 0.072 based on the flow scales around the channel ribs ($U = 1$ m/s, $H = 2$ mm). Both the Stokes and Reynolds numbers for this flow were dynamically similar to roughly 1 μm diameter sand particles transported by compressor bypass air into a turbine internal cooling geometry.

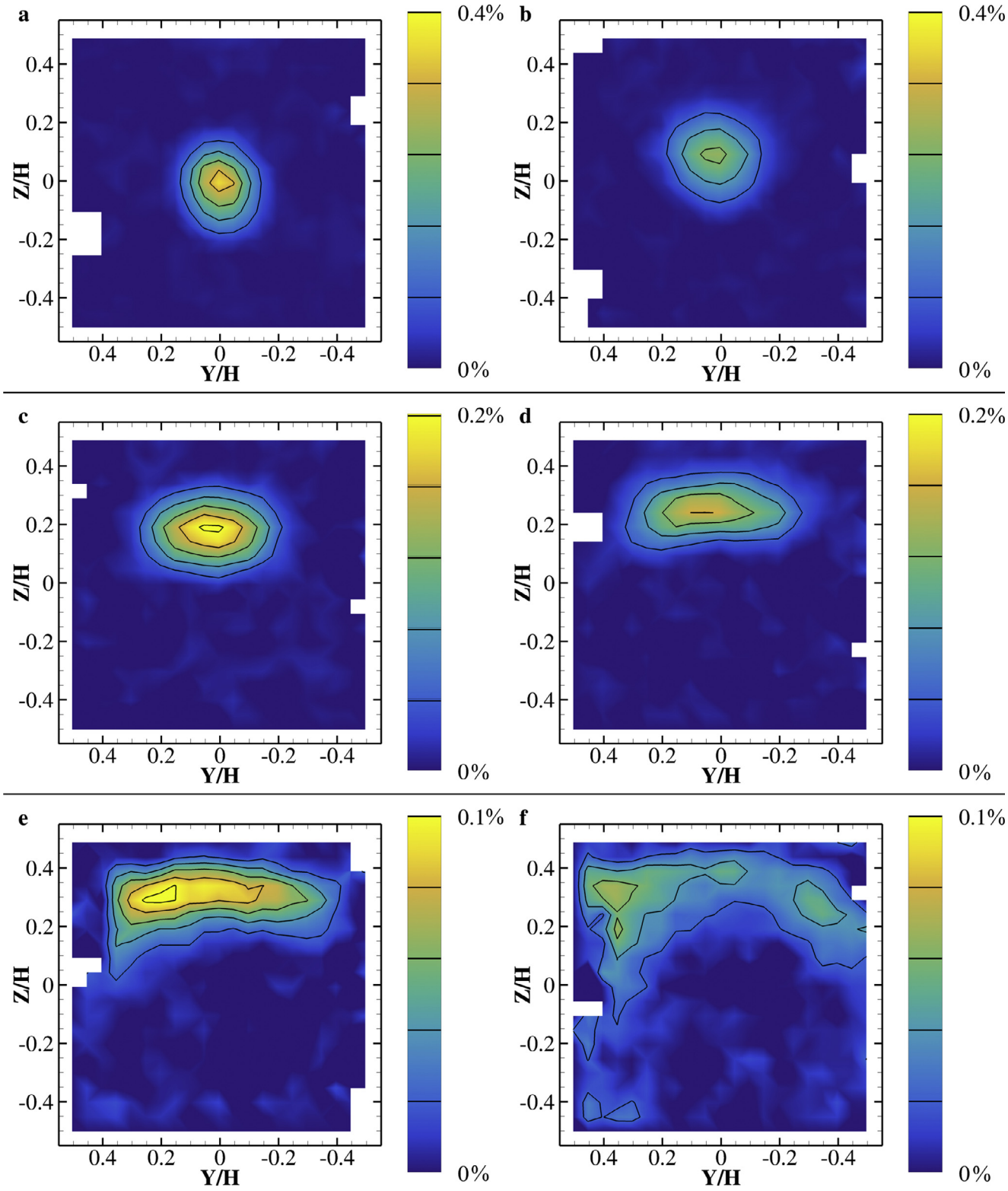

Fig. 9. Contours of particle concentration (ϕ_v) in streamwise slices. Color contours range from 0% to 0.4% for $X/D = 1, 2$ (a, b), 0% to 0.2% for $X/D = 3, 4$ (c, d), and 0% to 0.1% for $X/D = 5, 6$ (e, f). Lines denote the same levels as shown in contour legends.

5.2. Results

TE values and fitting procedures for the ribbed channel streak data were identical to those described for the calibration flow. Twenty scans were averaged for each of the particle-laden and no-particle flows, for a total of 40 scans. Data were obtained on a 1 mm^3 isotropic grid. The theoretical value of $A = 61.4\,ms^{-1}$ was used to convert measured decay rates into particle concentration values; the only region of known concentration was the injector, which was too small to be used for in-situ calibration. Fig. 9 shows color contours of ϕ_v in the first passage of the ribbed channel flow at streamwise positions of $X/H = 1, 2, 3, 4, 5,$ and 6. The Y and Z coordinate axes are normalized by the channel

height, and the images are oriented as if looking from the upstream end of the channel. The blanked rectangular regions along the left and right walls correspond to approximate locations of the ribs at the intersection with each slice.

Several interesting transport phenomena are immediately visible from the data. In Fig. 9a, located at $X/H = 1$, the particle streak is centered in the channel and has a roughly circular cross-section. Turbulent mixing has already lowered the peak concentration to just below 0.4% (40% of the injected concentration) between $X/H = 0$ and 1. The maximum ϕ_v in the streak will continue to drop throughout the channel, but at a slower rate of roughly a factor of two decrease in ϕ_v per $2H$ increment in X (c.f. Fig. 9a, c, and e). The more rapid drop in peak ϕ_v just after injection is likely due to strong turbulence generated behind the blunt trailing edge of the injector.

The secondary flows in the ribbed channel dominate the mean transport of the particle streak. As the ribs along the walls at $Y/H = +0.5$ and -0.5 sweep fluid downward and reduce its streamwise velocity, the central fluid is accelerated and pushed up; two counter-rotating vortex cells are ultimately formed along the left and right halves of the channel. Fig. 9b–d show the particle streak being transported in the $+Z$ direction by the common-up flow in the center of the channel between $X/H = 2$ and 4. The streak is also observed to spread towards the $+Y$ and $-Y$ walls beginning at $X/H = 3$. A wide, coherent streak is still present at $X/H = 5$ (Fig. 9e); here, the streak has not yet been entrained into the inter-rib space where fluid is being swept downward. This changes dramatically by $X/H = 6$ (Fig. 9f), where the streak has broken up into multiple local ϕ_v maxima and high-concentration regions are present in the inter-rib gaps.

It is also important to note the distinct asymmetry of the streak: both Fig. 9e and f show significantly higher particle concentrations present nearer the left wall. At $X/H = 5$, ϕ_v values in the left half-channel are nearly double those in the right. As the streak breaks up at $X/H = 6$, more particles are collected into the left rib gaps than the right. The high-concentration region in the bottom-left corner of Fig. 9f shows that some particles have already been swept down by the upstream ribs on the left side. Close inspection of the data reveals that the onset of this asymmetry is visible as far upstream as $X/H = 2$, where the streak is centered at around $Y/H = +0.05$.

The asymmetric behavior of the particle streak results from the staggered arrangement of the ribs, where the furthest upstream rib, located on the left wall, induces a slightly larger swirling cell in the left half-channel. The reader is directed to Borup et al. (2017), where the full 3D, 3-component velocity field has been reported, for evidence of this asymmetry in the flow. In particular, streamlines seeded at the injector exit show the same tendency to drift towards the wall with upstream ribs, indicating that this is not a gravitational effect limited to the particle-laden streak. A smoothed isosurface drawn at $\phi_v = 0.024\%$, shown in Fig. 10 as viewed from the channel centerline at $X/H = 3$, highlights the strong preference for particles to sweep down between ribs on the left side of the channel. Although the streak is ultimately broken up by the ribs, a high-concentration region can be seen to persist even to $X/H = 10$, returning to the centerline as the flow approaches the bend.

The quantitative images in Fig. 9 and 3D visualization in Fig. 10 highlight the unique analysis that can be performed with an MRP data set. The strong asymmetry, although immediately apparent upon looking at the data, would be difficult to predict based on intuition alone. In addition, because of the well-defined inlet boundary conditions and availability of fully 3D particle concentration and 3-component velocity data, the results obtained in this geometry would be well suited for validating computational techniques for simulating particle-laden turbulent flows.

6. Conclusions

Magnetic Resonance Imaging was used to make quantitative measurements of the signal decay rate on a 3D Cartesian grid in both flowing and gel suspension systems, and to explore the signal magnitude in the neighborhood of a single stainless steel particle suspended in an otherwise particle-free gel. In the single-particle gel, significant signal loss was observed not only in the voxel containing the particle, but in the neighboring voxels on all sides. The spatial extent of signal loss was in good agreement with theoretical predictions. The relevant equations were used in subsequent experiments to ensure that a particle's region of influence was limited to a sub-voxel distance. These equations can be applied easily in any future studies.

The signal decay rate was measured in gel suspensions of glass, bismuth, graphite, and titanium powders, each with mean particle diameters on the order of 50 μm. In all cases, good linearity was observed in the calibration between R_2^*, the signal decay, and ϕ_v, the particle volume fraction. The differing properties and calibration constant, A, for these materials required them to be imaged at higher (glass) and lower (titanium, graphite) volume fractions. Thus, in future MRP experiments the type of particle could be varied based on the desired range of concentrations (e.g., glass would be suitable for denser suspensions).

Theoretical predictions for A were made according to the model of Yablonskiy and Haacke (1994), which is based upon dephasing of the hydrogen proton spins due to the magnetic field disturbance surrounding each particle. The measured value of A agreed to within 5% of the theory for graphite and titanium, but was a factor two larger than predicted for the glass powder. Because glass has relatively low magnetic susceptibility, it is likely that additional effects not captured in the theory play a more central role. Further study on the signal change due to low-susceptibility particles is needed before these can be used reliably with the MRP protocol.

The calibration between $R_{2,part}^*$ (the particle-induced signal decay rate) and ϕ_v for titanium particles was explored in a turbulent, square channel flow with a uniform particle distribution. This flow was produced by rapid injection and mixing of particles into a square channel flow. The Reynolds number of the flow was varied from 6300 to 12,200 to assess whether A would be independent of the flow rate in a fully turbulent regime. Particle volume fractions ranged from 0.1% to 0.9% for the low-Re flow and 0.05% to 0.2% for the high-Re flow.

Across the bulk of the channel, the measured calibration constant, A, was independent of the Reynolds number and agreed within 5% of the theoretical predictions. While preferential concentration of the particles by turbulence was expected, it did not seem to alter A throughout most of the flow. Noise in the calibration data was used to estimate the dynamic range for MRP. An SNR greater than 5 may be expected for volume fractions from 0.05% to 1.5% in future, full-length experiments; strong turbulence may decrease SNR at both extremes, while a shorter averaging time or higher imaging resolution will mostly degrade the low-concentration end of the range.

Lower values of A were observed in the upstream region of the channel, with the deviation from theory more significant for the high-Re case. Several potential rationales for this discrepancy were presented, with the two most probable causes being inflow effects (commonly seen in other MRI-based techniques) and the presence of large-scale structures in the pin wake region. Further study is merited to determine the precise cause, as the accuracy of future measurements depends on a precise understanding of where A can be assumed constant and where it may tend to vary.

In a demonstration case, a streak of 1% titanium particles by volume was injected along the centerline of a square channel flow with angled ribs. The particle streak was observed to follow the counterrotating swirling cells produced by the ribs, first traveling up along the channel centerplane before being stretched across the channel width and swept downwards between pairs of ribs. A weak asymmetry in the swirling structures, generated by the staggered arrangement of the ribs, caused the majority of the particles to sweep down along one of the two ribbed walls. The fully 3D nature of the MRP data set facilitated a precise

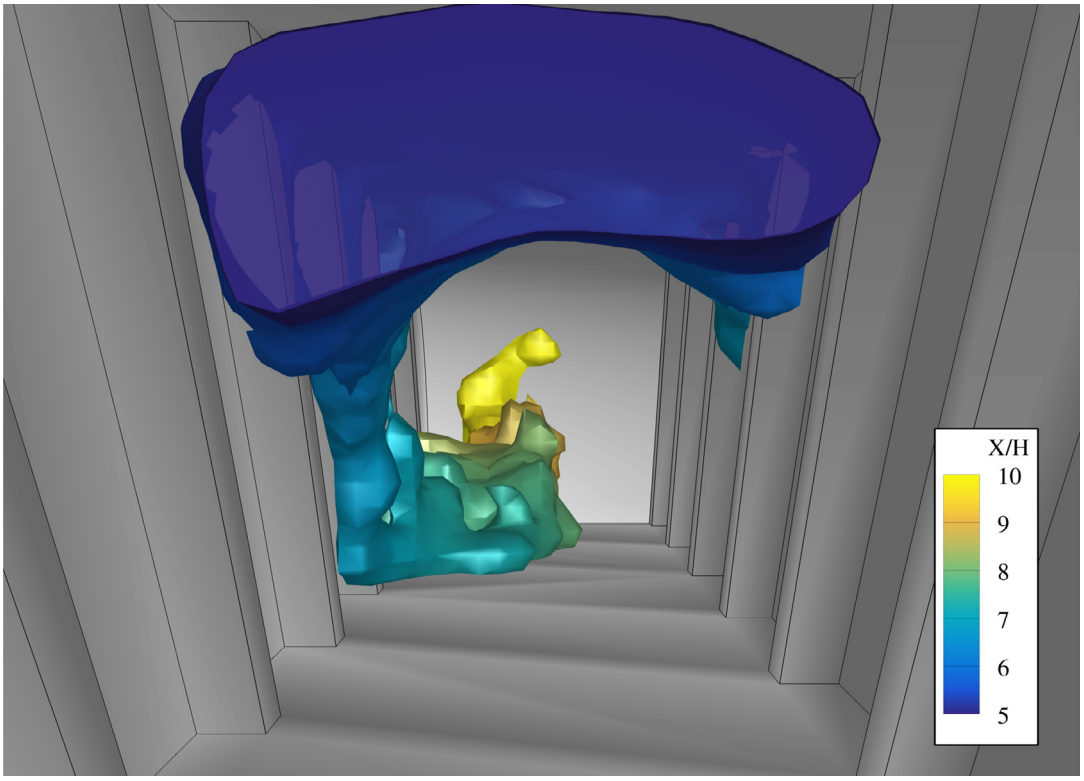

Fig. 10. A perspective view inside the channel, looking downstream from $X/H = 3$, shows a smoothed isosurface at $\phi_v = 0.024\%$ from $X/H = 5$ to 10. The staggered arrangement of the ribs, with the left ribs placed further upstream, causes the majority of particles to be swept down along the left wall. The isosurface is colored by streamwise location (X/H) to assist in visualizing the 3D shape.

understanding of this rather unusual flow.

Based on the results of these building-block experiments, the physics of MRP are well understood and the method can be applied across a wide range of turbulent multiphase flow systems. Two primary limitations exist for MRP at this stage. First, only mean concentration data have been measured to date. However, advanced MRI sequences have recently been used to acquire single component, 2D velocity data at a frequency of ~ 25 Hz; similar sequences could be applied to measure particle concentration at a comparable temporal resolution, based on the physical understanding behind MRP. Second, because MRP requires the use of water as the working fluid, particle aerodynamic time constants are constrained to O(1 ms). This places some limitation on the achievable Stokes number, as either high velocities (>1 m/s) or small length scales (<1 mm) are required to achieve a Stokes number of order unity. However, the SGTIP example presented here shows that measurable, physically significant inertial effects can exist even for centimeter-size channels.

Despite these early-stage limitations, the MRP diagnostic maintains the significant advantage of existing MRI-based techniques over probe and laser measurements, namely, the ability to quickly gather a 3D data set for complex geometries where optical access is difficult or impossible to achieve. This makes MRP a powerful tool for the study of application-specific flows across a number of arenas, from advanced engineering systems to biological flows. MRP also allows accurate quantification of the 3D volume fraction for dense flows of O(1%) particles by volume, with even higher loadings possible based on the choice of particle material. Furthermore, the three dimensional data sets produced by MRP are well suited for validation of computational modeling approaches, where accurate prediction of multiphase flows is still far from guaranteed in all but the highest fidelity simulations.

Acknowledgments

This work was supported through National Science Foundation (NSF) EAGER grant #CBET-1662422. Daniel Borup was supported jointly by an NSF Graduate Research Fellowship (grant #DGE-114747) and Stanford Office of Technology Licensing Graduate Fellowship. The authors are also grateful for the use of MRI facilities at the Richard M. Lucas Center for Imaging at Stanford University.

Supplementary material

Supplementary material associated with this article can be found, in the online version, at doi:10.1016/j.ijheatfluidflow.2018.04.006.

References

Akilli, H., Levy, E., Sahin, B., 2001. Gas–solid flow behavior in a horizontal pipe after a 90 vertical-to-horizontal elbow. Powder Technol. 116 (1), 43–52.

Banko, A.J., Coletti, F., Schiavazzi, D., Elkins, C.J., Eaton, J.K., 2015. Three-dimensional inspiratory flow in the upper and central human airways. Exp. Fluids 56 (6), 117.

Bendat, J.S., Piersol, A.G., 2011. Random Data: Analysis and Measurement Procedures. 729 John Wiley & Sons.

Benson, M.J., Elkins, C.J., Mobley, P.D., Alley, M.T., Eaton, J.K., 2010. Three-dimensional concentration field measurements in a mixing layer using magnetic resonance imaging. Exp. Fluids 49 (1), 43–55.

Berruti, F., Pugsley, T.S., Godfroy, L., Chaouki, J., Patience, G.S., 1995. Hydrodynamics of circulating fluidized bed risers: a review. Can. J. Chem. Eng. 73 (5), 579–602. http://dx.doi.org/10.1002/cjce.5450730502.

Borup, D.D., Elkins, C.J., Eaton, J.K., 2017. Transport of microparticles in a turbulated serpentine passage. ASME Turbo Expo 2017: Turbomachinery Technical Conference and Exposition. American Society of Mechanical Engineers. Paper number 63491.

Chang, S., Elkins, C., Alley, M., Eaton, J., Monismitha, S., 2009. Flow inside a coral colony measured using magnetic resonance velocimetry. Limnol. Oceanogr. 54 (5), 1819–1827.

Coletti, F., Borup, D., Elkins, C., Eaton, J., 2014. Measuring fluid, scalar, and particle transport in internal flows using medical imaging. 17th International Symposium on Applications of Laser Techniques to Fluid Mechanics.

Coletti, F., Muramatsu, K., Schiavazzi, D., Elkins, C.J., Eaton, J.K., 2014. Fluid flow and

scalar transport through porous fins. Phys. Fluids 26 (5), 055104.
Dixon, W.T., Blezek, D.J., Lowery, L.A., Meyer, D.E., Kulkarni, A.M., Bales, B.C., Petko, D.L., Foo, T.K., 2009. Estimating amounts of iron oxide from gradient echo images. Magn. Reson. Med. 61 (5), 1132–1136.
Dunn, M.G., Padova, C., Moller, J.E., Adams, R.M., 1987. Performance deterioration of a turbofan and a turbojet engine upon exposure to a dust environment. J. Eng. Gas Turbines Power 109 (3), 336–343.
Eaton, J.K., Fessler, J., 1994. Preferential concentration of particles by turbulence. Int. J. Multiphase Flow 20, 169–209.
Elkins, C.J., Alley, M.T., 2007. Magnetic resonance velocimetry: applications of magnetic resonance imaging in the measurement of fluid motion. Exp. Fluids 43 (6), 823–858.
Elkins, C.J., Markl, M., Iyengar, A., Wicker, R., Eaton, J.K., 2004. Full-field velocity and temperature measurements using magnetic resonance imaging in turbulent complex internal flows. Int. J. Heat Fluid Flow 25 (5), 702–710.
Fong, W., 2005. Handbook of mri pulse sequences. Med. Phys. 32 (5). 1452–1452.
Girard, O., Ramirez, R., McCarty, S., Mattrey, R., 2012. Toward absolute quantification of iron oxide nanoparticles as well as cell internalized fraction using multiparametric mri. Contrast Media Mol. Imaging 7 (4), 411–417.
Griffin, D.W., Kellogg, C.A., Shinn, E.A., 2001. Dust in the wind: long range transport of dust in the atmosphere and its implications for global public and ecosystem health. Global Change Human Health 2 (1), 20–33.
Grundmann, S., Wassermann, F., Lorenz, R., Jung, B., Tropea, C., 2012. Experimental investigation of helical structures in swirling flows. Int. J. Heat Fluid Flow 37, 51–63.
Gu, H., Gong, H., Dilip, J., Pal, D., Hicks, A., Doak, H., Stucker, B., 2014. Effects of powder variation on the microstructure and tensile strength of Ti6Al4V parts fabricated by selective laser melting. Proceedings of the 25th Solid Freeform Fabrication Symposium. pp. 470–483.
Kalt, P.A., Birzer, C.H., 2005. Calibrations for planar laser nephelometry in densely seeded two-phase flows. Fourth Australian Conference on Laser Diagnostics in Fluid Mechanics and Combustion. pp. 73–76.
Kalt, P.A., Birzer, C.H., Nathan, G.J., 2007. Corrections to facilitate planar imaging of particle concentration in particle-laden flows using mie scattering, part 1: collimated laser sheets. Appl. Opt. 46 (23), 5823–5834.
Kalt, P.A., Nathan, G.J., 2007. Corrections to facilitate planar imaging of particle concentration in particle-laden flows using mie scattering. part 2: diverging laser sheets. Appl. Opt. 46 (29), 7227–7236.
Kleinstreuer, C., Zhang, Z., 2010. Airflow and particle transport in the human respiratory system. Annu. Rev. Fluid Mech. 42, 301–334.
Kuhlpeter, R., Dahnke, H., Matuszewski, L., Persigehl, T., von Wallbrunn, A., Allkemper, T., Heindel, W.L., Schaeffter, T., Bremer, C., 2007. R2 and r2* mapping for sensing cell-bound superparamagnetic nanoparticles: in vitro and murine in vivo testing. Radiology 245 (2), 449–457.
Lau, T.C., Nathan, G.J., 2016. The effect of stokes number on particle velocity and concentration distributions in a well-characterised, turbulent, co-flowing two-phase jet. J. Fluid Mech. 809, 72–110.
Lee, J., Yang, B., Song, S., 2015. 3D visualization of flow inside carpet using magnetic resonance velocimetry. Korean Society of Mechanical Engineers 70th Anniversary Conference. The Korean Society of Mechanical Engineers, pp. 121–124.
Liu, C., Kiger, K.T., 2016. Multi-camera PIV imaging in two-phase flow for improved dispersed-phase concentration and velocity calculation. 18th International Symposium on Applications of Laser and Imaging Techniques to Fluid Mechanics.
Mastin, L., Guffanti, M., Servranckx, R., Webley, P., Barsotti, S., Dean, K., Durant, A., Ewert, J., Neri, A., Rose, W.I., et al., 2009. A multidisciplinary effort to assign realistic source parameters to models of volcanic ash-cloud transport and dispersion during eruptions. J. Volcanol. Geotherm. Res. 186 (1), 10–21.
Oshinski, J.N., Ku, D.N., Pettigrew, R.I., 1995. Turbulent fluctuation velocity: the most significant determinant of signal loss in stenotic vessels. Magn. Reson. Med. 33 (2), 193–199.
Pan, G., Meng, H., 2003. Digital holography of particle fields: reconstruction by use of complex amplitude. Appl. Opt. 42 (5), 827–833.
Papanicolaou, A.T.N., Elhakeem, M., Krallis, G., Prakash, S., Edinger, J., 2008. Sediment transport modeling reviewcurrent and future developments. J. Hydraul. Eng. 134 (1), 1–14.
Parker, D.L., Gullberg, G.T., 1990. Signal-to-noise efficiency in magnetic resonance imaging. Med. Phys. 17 (2), 250–257.
Robson, P., Hall, L., 2005. Identifying particles in industrial systems using mri susceptibility artefacts. AlChE J. 51 (6), 1633–1640.
Ryan, K.J., Coletti, F., Elkins, C.J., Dabiri, J.O., Eaton, J.K., 2016. Three-dimensional flow field around and downstream of a subscale model rotating vertical axis wind turbine. Exp. Fluids 57 (3), 38.
Scarano, F., 2012. Tomographic piv: principles and practice. Meas. Sci. Technol. 24 (1), 012001.
Schenck, J.F., 1996. The role of magnetic susceptibility in magnetic resonance imaging: MRI magnetic compatibility of the first and second kinds. Med. phys. 23 (6), 815–850.
Singh, S., Tafti, D., Reagle, C., Delimont, J., Ng, W., Ekkad, S., 2014. Sand transport in a two pass internal cooling duct with rib turbulators. Int. J. Heat Fluid Flow 46, 158–167.
Sinnott, M., Cleary, P.W., Morrison, R.D., 2011. Slurry flow in a tower mill. Miner. Eng. 24 (2), 152–159.
Sinnott, M.D., Cleary, P.W., Harrison, S.M., 2017. Peristaltic transport of a particulate suspension in the small intestine. Appl. Math. Model. 44, 143–159.
Spirnak, J., Samland, M., Tremont, B., McQuirter, A., Williams, E., Benson, M., Poppel, B.V., VerHulst, C., Elkins, C., Burton, L., Eaton, J., Owkes, M., 2016. Validation of magnetic resonance thermometry through experimental and computational approaches. AIAA Propulsion and Energy Forum.
Tang, L., Wen, F., Yang, Y., Crowe, C., Chung, J., Troutt, T., 1992. Self-organizing particle dispersion mechanism in a plane wake. Phys. Fluids A 4 (10), 2244–2251.
Willert, C., Gharib, M., 1992. Three-dimensional particle imaging with a single camera. Exp. Fluids 12 (6), 353–358.
Yablonskiy, D., Haacke, E.M., 1994. Theory of NMR signal behavior in magnetically inhomogeneous tissues: the static dephasing regime. Magn. Reson. Med. 32 (6), 749–763.